AIAA JOURNAL
Vol. 45, No. 11, November 2007

Aero-Optical Resolution Robustness in Turbulent Separated Shear Layers at Large Reynolds Numbers

Fazlul R. Zubair* and Haris J. Catrakis†
University of California, Irvine, Irvine, California 92697-3975

DOI: 10.2514/1.30742

The effects of spatial imaging resolution on a computed aero-optical interaction parameter are examined using experimental images of the refractive-index field in turbulent compressible separated shear layers. Spatial coarse-graining of refractive-index-field images are conducted at various resolutions and the resulting aero-optical aberrations are evaluated. Evidence is presented for robustness of the aero-optical interactions to resolution reduction, indicating that the large scales are dominant relative to the small scales. The extent to which the large scales dominate the small scales is quantified in terms of a measure of the aero-optical contributions as a function of the resolution scale. Implications of the observed resolution-scale robustness are suggested for aero-optical investigations and applications in terms of the practical benefits that result from the significant reduction in the amount of refractive-index-field information required.

I. Introduction

THE study of directed energy propagation through turbulent shear layers is an important fundamental problem in aero-optics [1,2]. One of the practical goals in the study of aero-optics is to develop closed-loop systems for suppression or organization of large-scale structures in turbulent flowfields. To develop such systems, the basic relationship between the turbulent-generated refractive-index fields and the corresponding wave-front behavior of the directed energy systems must be understood. Over the years, many advances have been made experimentally, computationally, and theoretically that have increased our understanding of the nature of turbulent fields [3–9]. Through these advances, it became clear that the determination of the resultant aero-optical interactions and distortions caused by the dominant flow mechanisms are important concepts for many basic and applied aero-optics problems [1] and can be used to develop accurate methods for determining the behavior of large Reynolds number turbulent flows [8,9].

An improved understanding of the interfacial behavior, which governs the basic physical interactions between the propagating optical wave fronts and the turbulent flows across the refractive-index-fluid interfaces, is required [2]. Direct imaging of the turbulent refractive fields and interfaces using techniques such as laser-induced fluorescence is useful to examine the aero-optical interactions, as we have shown in a companion study [10], but at high resolution this requires expensive cameras and adequate bandwidth to capture, transfer, and process the data. To reduce the expense and the bandwidth, lower-resolution imaging would be highly desirable if appropriate, that is, if the aero-optical interactions are dominated by large-scale flow features, which is an idea for which some supporting evidence can be found in previous works [5,8,9,11]. The present work focuses on the effects of resolution reduction on the identification of large-scale aero-optical phenomena. In addition to experimental savings in bandwidth and equipment, these resolution effects would provide important advantages to the computational and theoretical communities. Resolution reduction in the computational sense can directly result in reduction in computation time or processor power with the use of large-eddy-simulation approaches. This can significantly reduce the cost of running a simulation or allow for more simulations to be run in a similar time period. Additionally, the theoretical community has a strong interest in physical modeling of multiresolution and multiscale aspects of scalar turbulent fields and interfaces, such as refractive fields and interfaces. This can include the analysis of self-similar fractals [12] at small scales or generalized fractals [2] at large scales.

In the present work, we examine the extent to which resolution reduction affects the aero-optical interactions and aberrations in high Reynolds number separated compressible shear layers. Basic aspects of the aero-optical interactions were investigated in our companion study, reported previously [10]. In Sec. II, the variable-pressure flow facility at the University of California, Irvine and the aero-optical imaging technique are briefly described, which are used to generate and capture images of turbulent shear layers. The rest of the section will contain a detailed explanation of the coarse-graining method used in the present study. The method we use for reduction of resolution relies on spatial-averaging combined with biquadratic B-spline interpolation, to preserve continuous gradients of the coarse-grained refractive-index field, which are essential for extracting coarse-grained refractive interfaces. In Sec. III, results of the coarse-graining of the experimental laser-induced fluorescence refractive-field images are presented with the corresponding results of computationally derived laser wave fronts propagated through the experimental images. Results are shown using the interaction optical path difference (IOPD) and the total optical path difference (OPD), to be defined later, for various resolution-scale reductions, to quantitatively assess the extent of resolution robustness. Finally, implications of the observed behavior for aero-optical studies are suggested in terms of the practical benefits associated with the reduction in the amount of refractive-field information needed for certain applications.

II. High-Resolution Database and Coarse-Graining Method

In this section, we will describe the coarse-graining approach and multiresolution representation that were used to examine the dependence of the experimentally obtained refractive-index fields on resolution-scale effects. We explore the resolution dependence (i.e., robustness or sensitivity) of the laser aberrations associated with the refractive-index fields by computationally coarse-graining refractive-index measurements. The refractive-index fields, before

Presented as Paper 0325 at the 45th AIAA Aerospace Sciences Meeting and Exhibit, Reno, NV, 8–11 January 2007; received 28 February 2007; revision received 9 July 2007; accepted for publication 3 August 2007.

*Graduate Student, Mechanical and Aerospace Engineering; fazlul.zubair@uci.edu. Member AIAA.

†Associate Professor, Mechanical and Aerospace Engineering; catrakis@uci.edu. Member AIAA (Corresponding Author).

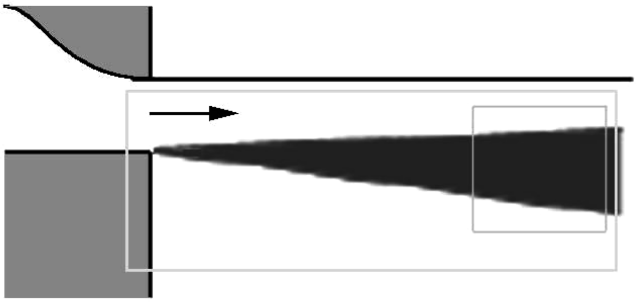

Fig. 1 Schematic showing the separated shear-layer geometry. The rectangular outline indicates the whole-field region of the shear layer. The square outline indicates the far-field region of the shear layer that is imaged using laser-induced fluorescence.

coarse-graining, are high-resolution images that have been experimentally obtained using the variable-pressure flow facility at the University of California, Irvine. A description of the facility and experimental procedure is available in detail in our previous work [10]. A brief summary of the experimental approach is stated in this section, for completeness.

The main components of the laboratory facility are two high-pressure vessels used in all of our experiments to generate and contain the turbulent flows. The main pressure vessel can contain gas pressures up to ∼300 psi or ∼20 atm. The reservoir vessel for the system can hold pressures up to ∼3, 000 psi or ∼200 atm. Flow is generated via a blowdown wind tunnel contained within the main pressure vessel. The flow is driven by charging the reservoir tank to ∼135 psi or ∼9 atm and filling the main pressure vessel to ∼45 psi or ∼3 atm. The flow is created by opening a fast-acting valve between the two pressure vessels. Through the use of a wall oriented at 90 deg to the bottom wall of the nozzle section in the wind tunnel, a turbulent separated shear layer is created, as shown in Fig. 1. For the flow conditions used in this experiment, the Reynolds number based on the visual thickness of the flowfield is $Re \sim 6 \times 10^6$ and the convective Mach number is $M_c \sim 0.4$. The large scale of the shear layer at the imaging location is the visual thickness, which is $L \sim 0.1$ m. From Kolmogorov scaling, the smallest scale of the shear layer is $\lambda_K = L/Re^{3/4} \sim 0.1/(6 \times 10^6)^{3/4} \sim 1$ μm. Thus, the range of scales spans approximately five decades, whereas our imaging resolution captures only the three upper decades because the pixel resolution scale is ∼0.1 mm. Additionally, the aero-optics variable-pressure flow facility at the University of California, Irvine allows for experiments to be conducted at elevated test-section pressures, to maximize the signal-to-noise ratio of the flow images.

The shear-layer images shown in this study were captured using laser-induced florescence that is generated by the interaction of acetone vapor, which was molecularly mixed with pure air in the reservoir vessel, and an ultraviolet laser sheet. Preparation of the purely gaseous air/acetone mixture was done using the bubbling method [13] described in other work. The laser source used is an ultraviolet beam generated from a pulsed Nd:YAG laser (Spectra Physics Model INDI 40-10), which was measured to output ∼70 mJ per pulse at a wavelength of 266 nm. The laser beam is turned into a laser sheet, with a thickness of ∼150 μm, through use of a cylindrical lens, which is then propagated through the quartz windows of the pressure vessel and into the separated shear layer formed in the test section. The laser sheet excites the acetone vapor in the shear layer to generate a visible (blue) fluorescence, which is recorded with a high-resolution digital intensified charge-coupled device (ICCD) camera. The digital camera system employed is an ICCD camera by Stanford Photonics (Mega-10Z) with enhanced sensitivity in the blue spectrum. Images generated from these experiments are then coarse-grained and analyzed using the interaction optical path difference functions, described at the end of this section, to determine the effects that resolution reduction has on the identification of aero-optical interactions.

The study of the multiresolution aspects of the aero-optical interactions requires the ability to examine an image at different resolutions. To accomplish this, coarse-graining was performed on the high-resolution (1000 by 1000 pixels) 2-D refractive-index-field data using biquadratic B-splines [14]. To ensure that the resolution-reduction method would be consistent with the use of lower-resolution imaging, we use a resolution-reduction approach that preserves a continuous refractive-index field and refractive-index gradient. Let us define each set of high-resolution refractive-index-field values as a array with the following notation:

$$n(x_i, y_j) \tag{1}$$

at $x = x_i$ and $y = y_j$, where $i = 1, 2, \ldots, N_x$ and $j = 1, 2, \ldots, N_y$, with N_x and N_y being the number of pixels in x and in y, respectively.

The coarse-grained refractive-index-field value can then be described with the following notation:

$$\hat{n}_q(x_k, y_l) \tag{2}$$

at $x = x_k$ and $y = y_l$, where $k = 0, 1, \ldots, N_x\alpha$ and $l = 0, 1, \ldots, N_y\alpha$, and where α is a parameter that we denote as the resolution-reduction parameter. This resolution-reduction factor is related to the number of pixels in the reference-resolution image and the number of pixels of the coarse-grained image. We define the resolution-reduction factor α as

$$\alpha = \frac{N}{N_{\text{ref}}} \tag{3}$$

where N_{ref} is the number of pixels in the reference-resolution image (i.e., corresponding to the original resolution of the image data available). This means that α is a discrete variable ranging from a value of 0 to 1. The biquadratic B-spline interpolated field value will be denoted as follows:

$$\tilde{n}_\alpha(x_i, y_j) \tag{4}$$

at $x = x_i$ and $y = y_j$, where $i = 1, 2, \ldots, N_x$ and $j = 1, 2, \ldots, N_y$, with N_x and N_y being the number of pixels in x and in y, respectively, which is the same number of pixels as in the original image.

To coarse-grain (i.e., to reduce the effective resolution of) the high-resolution images, two processes were used to ensure a continuous image and the refractive-index boundaries. In the first process, which entails coarse-graining the image through use of averaging, $n(x_i, y_j)$ is converted to $\hat{n}_\alpha(x_i, y_j)$. The goal of this process is to reduce the number of pixels in the images by means of spatial-averaging, to be consistent with what the effect would be if one were to employ a lower-resolution camera. For example, if a 200 by 200 pixel image needed to be reduced to a 5 by 5 pixel image, each 40 by 40 pixel segment of the original image would be averaged to create 1 pixel in the reduced-resolution image. Therefore, $\hat{n}_\alpha(x_i, y_j)$ is related to $n(x_i, y_j)$ using the following relationship:

$$\hat{n}(x_i, y_j) = \mathcal{A}n(x_i, y_j) \tag{5}$$

where $\mathcal{A}$ is the spatial-averaging filter operator, which is performed as follows:

$$\hat{n}(x_k, y_l) = \frac{\sum_{i=x_{k/\alpha-1/\alpha}}^{x_{k/\alpha}} \sum_{j=y_{l/\alpha-1/\alpha}}^{y_{l/\alpha}} n(x_i, y_j)}{[1/(1-\alpha)]^2} \tag{6}$$

Note, however, that even though this coarse-graining approach yields averaged pixels, it can produce discontinuous gradients in the refractive-index field and thus discontinuities in the slope of the refractive interfaces. The next step is to use biquadratic B-splines to ensure that the interfaces are kept continuous. Similar to the previous relationship, the original image is averaged and reduced to a lower number of pixels. Biquadratic B-splines are then used to smooth out the image to maintain the location and size of the refractive-index interfaces. A key difference between B-splines and normal splines is that the latter are not localized, whereas B-splines are localized interpolations. Splines can dramatically change the values at pixels far away from a change or error in pixel value; however, B-splines

have the advantage of not being this sensitive. Because B-splines are local, any changes or errors in some pixels do not cause any change far away from the pixels. The following relation shows how $\tilde{n}_\alpha(x_i, y_j)$ is related to $\hat{n}_\alpha(x_i, y_j)$:

$$\tilde{n} = \mathcal{B}\hat{n} = \mathcal{B}\mathcal{A}n \tag{7}$$

$$\tilde{n}(x_i, y_j) \equiv \tilde{n}\left(\frac{i}{i_{\max}}k_{\max}, \frac{j}{j_{\max}}l_{\max}\right) = \frac{1}{4}yx^T : \hat{N} \tag{8}$$

where the colon denotes the double scalar product, and where $\hat{N}$ is a 3 by 3 matrix defined as follows:

$$\hat{N}_{a,b} = \hat{n}(\boldsymbol{x}_k - 2 + a, \boldsymbol{y}_l - 2 + b) \tag{9}$$

where $a = 1, 2, 3$; $b = 1, 2, 3$; and $\boldsymbol{x}$ and $\boldsymbol{y}$ are vectors defined as follows:

$$\boldsymbol{x}^T = [(1.5 - \delta x_1)^2, (1.5 - 2(\delta x_2)^2, (1.5 + \delta x_3)^2] \tag{10}$$

$$\boldsymbol{y}^T = [(1.5 - \delta y_1)^2, (1.5 - 2(\delta y_2)^2, (1.5 + \delta y_3)^2] \tag{11}$$

where $\delta x_1 = (i/i_{\max})k_{\max} - (x_k - 1)$, $\delta x_2 = (i/i_{\max})k_{\max} - x_k$, $\delta x_3 = (i/i_{\max})k_{\max} - (x_k + 1)$, $\delta y_1 = (j/j_{\max})l_{\max} - (x_l - 1)$, $\delta y_2 = (j/j_{\max})l_{\max} - x_l$, and $\delta y_3 = (j/j_{\max})l_{\max} - (x_l + 1)$, and where x_k is $(i/i_{\max})k_{\max}$ and $(j/j_{\max})l_{\max}$ rounded to the nearest integer.

Figure 2 shows a 200 by 200 pixel region of a shear layer that is coarse-grained to lower resolutions. The original image was subjected to biquadratic B-splines, which reduced the resolution to 20 by 20 and 5 by 5 pixels. It is evident in the images that the resolution-reduction technique results in continuous refractive-index fields and gradients.

These multiresolution images can now be analyzed to determine the effects of the shear layer on a laser beam. Knowledge of the refractive-index field is invaluable for evaluating beam behavior, such as determining optical-wave-front distortions and identifying the dominant fluid interfaces [5,8]. In this study, the eikonal equation of geometrical optics is used to computationally propagate an optical wave front through the experimentally captured refractive-index-field images. A full description of the interaction optical path difference computations can be found in previous studies [10]. The eikonal equation can be written in terms of the refractive-index field n and the optical path length (OPL) [15] as follows:

$$|\nabla(\mathrm{OPL})| = n \tag{12}$$

The solutions to this equation can easily be found by inverting and integrating along the entire individual ray paths. This corresponds to the total OPL integral that can be represented in terms of the refractive-index field, which can also be expressed as a total integral in terms of the local thickness of the refractive interfaces [9]. To study the aero-optical interactions, it is useful to consider the interaction optical path length (IOPL) which can be defined as the running integral of the refractive field and is a function of the partial distance along the laser path in the flow. An IOPD can then be defined from the IOPL, which can be used to quantitatively describe the beam distortion. The rms value of the IOPD can also be used give a quantitative measure of how distorted the entire beam is as it propagates through the shear layer. The following are the equations used in the analysis of the aero-optical interactions:

$$\mathrm{IOPD}\,(\ell, t) \equiv \mathrm{IOPL}(\ell, t) - \langle \mathrm{IOPL}(\ell, t)\rangle_{\mathrm{avg}} \tag{13}$$

where $\langle \mathrm{IOPL}(\ell, t)\rangle_{\mathrm{avg}}$ corresponds to the aperture-averaged IOPL value:

$$\mathrm{IOPD}_{\mathrm{rms}}(\ell, t) \equiv (\langle |\mathrm{IOPD}(\ell, t)|^2\rangle_{\mathrm{avg}})^{1/2} \tag{14}$$

The following section will show the results of the biquadratic B-splines on reference-resolution shear-layer images, as well as the results of the IOPD and $\mathrm{OPD}_{\mathrm{rms}}$ analysis on these images. Results will focus on the $\mathrm{OPD}_{\mathrm{rms}}$, defined as the total $\mathrm{OPD}_{\mathrm{rms}}$ value (or the $\mathrm{OPD}_{\mathrm{rms}}$ after the beam passes through the shear layer), to compare the integrated results of the aero-optical interactions with the laser sheet as a function of the resolution of the shear-layer images.

III. Multiresolution Results and Robustness

In this section, we examine the aero-optical effects associated with resolution reduction by conducting coarse-graining using the averaging filter and the B-spline interpolation filter applied to the laser-induced fluorescence images. As demonstrated in Fig. 2, some of the smaller features of the shear layer are visually smoothed out, leaving the large features dominant in the image. Figure 3 shows a reference-resolution shear-layer image and subsequent reductions of image resolution through the use of biquadratic B-splines. Figure 4 is a side-by-side comparison of the images in Fig. 3; however, in this figure, the refractive-index interfaces are extracted through computations of the concentration gradients. Notice that as the resolution of the image decreases, the smaller refractive-index interfaces disappear from the image, leaving only the large-scale interfaces.

Figures 5–7 show the corresponding IOPD plots and OPD profiles of the reference-resolution and reduced-resolution images of the turbulent shear layer depicted in Fig. 3. The IOPD surface plots in these figures describe the behavior of the wave front as it passes through the shear layer. The wave front computed through the experimental data is assumed to be initially undistorted, as seen by the flat profiles at the beginning of the IOPD plots. However, as the wave front starts to interact with the various refractive interfaces, it undergoes multiscale distortions until it exits the shear layer. The OPD profiles in Figs. 5–7 show the results of the wave-front distortions on the IOPD as it passes through the last part of the shear layer. Note that even with only 20 by 20 pixels, shown in Fig. 7, the final IOPD plot and OPD profile are similar to the corresponding plots at the reference resolution. The IOPD surface plots in these figures also serve to exemplify the point that as the resolution is reduced, distortions caused by the large features remain visible. The surface plots show that the small features, seen in the analysis of the reference-resolution image, are smoothed out and the resulting IOPD plots show the large wave-distortion features. Similarly, the OPD plots at the end of the shear layer shows the small features, seen in the reference-resolution plot, smoothed out in the reduced-resolution plots. Because these small features did not contribute much to the overall shape of the profile, the $\mathrm{OPD}_{\mathrm{rms}}$ value of the plots are very similar.

Figures 8 and 9 show plots of the percent change in the average $\mathrm{OPD}_{\mathrm{rms}}$ value (in normal and log scale, respectively) of several shear layers, randomly chosen from our database of approximately 20 images, with respect to the percent of resolution-scale reduction of the shear-layer images, defined as q_2. The parameter q_2 can be computed using the following equation:

$$q_2 = 1 - \alpha \tag{15}$$

where α is the resolution-reduction parameter introduced in Eq. (3) in Sec. II.

Percent change in $\mathrm{OPD}_{\mathrm{rms}}$ can be defined with the following equation:

$$\%\ \mathrm{OPD}_{\mathrm{rms}}\ \text{change} = \frac{|\mathrm{OPD}_{\mathrm{rms}}(\text{reference}) - \mathrm{OPD}_{\mathrm{rms}}(\text{coarse-grained})|}{\mathrm{OPD}_{\mathrm{rms}}(\text{reference})} \times 100 \tag{16}$$

where the reference $\mathrm{OPD}_{\mathrm{rms}}$ value was taken at the reference resolution and the coarse-grained value was taken at the lower resolution. The parameter q_2 is appropriate for describing a 2-D scale resolution reduction; however, similar parameters can also be defined in 1-D, 3-D, or space-time 4-D, as shown next:

$$q_1 = 1 - \sqrt{\alpha} \tag{17}$$

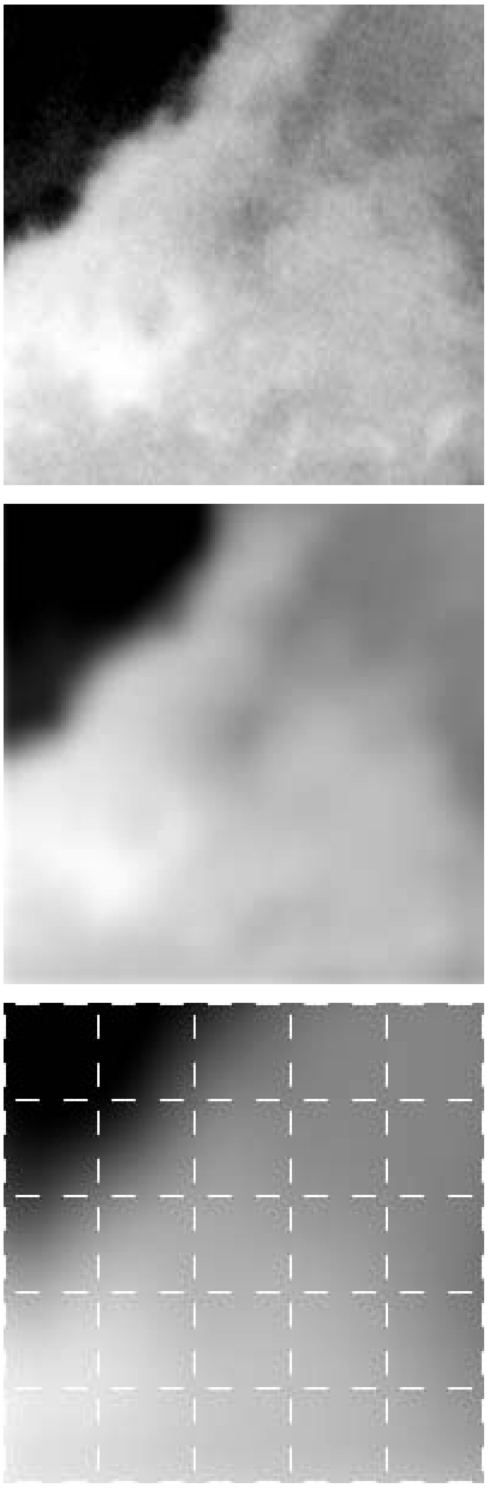

Fig. 2 Zoomed-in refractive-index-field region, extracted from a whole image, showing resolution reduction by coarse-graining using biquadratic B-splines; reference resolutions of (top) 200 by 200 pixels, (middle) 20 by 20 pixels, and (bottom) 5 by 5 pixels.

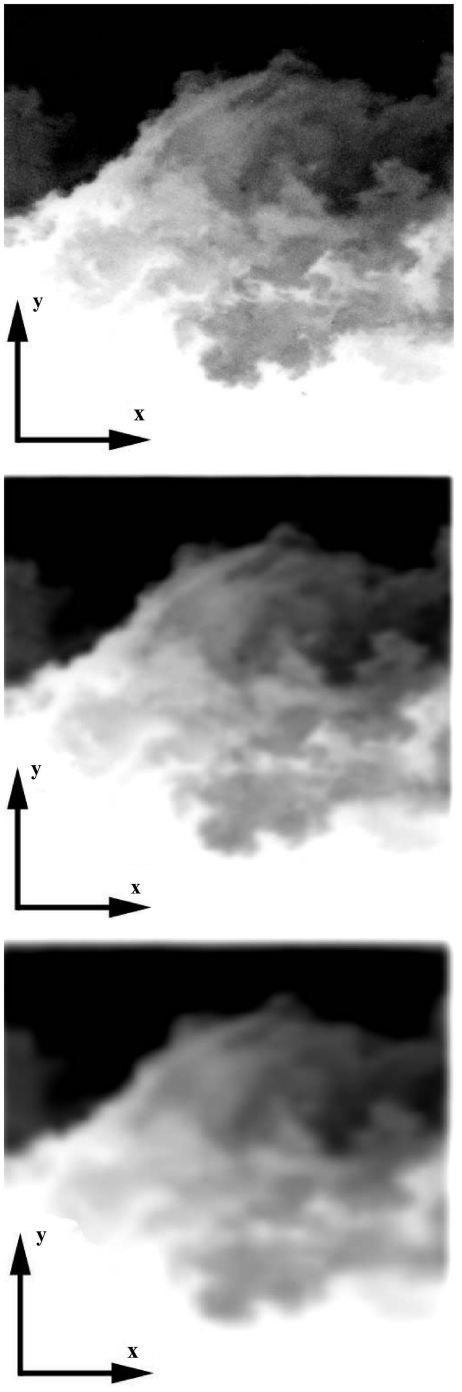

Fig. 3 Laser-induced florescence image of the refractive-index field of a turbulent shear layer subjected to coarse-graining to study multi-resolution effects. The laser sheet is propagated in the positive *y* direction (from the bottom to the top of the image). Reference-resolution images of (top) 800 by 800 pixels, (middle) 100 by 100 pixels, and (bottom) 50 by 50 pixels.

$$q_3 = 1 - \alpha^{3/2} \tag{18}$$

$$q_4 = 1 - \alpha^2 \tag{19}$$

where q_1, q_3, and q_4 are the 1-D, 3-D, or space-time 4-D refractive-field information-reduction quantities, respectively. For example, if the reference-resolution image had 1000 by 1000 pixels and a reduced-resolution image had 500 by 500 pixels, the reduced-resolution image would have a 25% reduction of the 2-D image resolution scale. This is because from 1000 by 1000 pixels to 500 by 500 pixels, one notices a reduction of total pixels from 10^6 to 250,000. It is from this notion that q_1, q_3, and q_4 are also defined as the percent of image information reduction. These parameters are shown in Figs. 10 and 11, in which the percent change in $\mathrm{OPD}_{\mathrm{rms}}$ is plotted (again in normal and log scale, respectively) with respect to the parameters q_1, q_2, q_3, and q_4. Note that the parameter q_1 can also be useful in addressing reductions of solely the temporal bandwidth, in cases in which refractive-field information is only available as a function of time at a single point location.

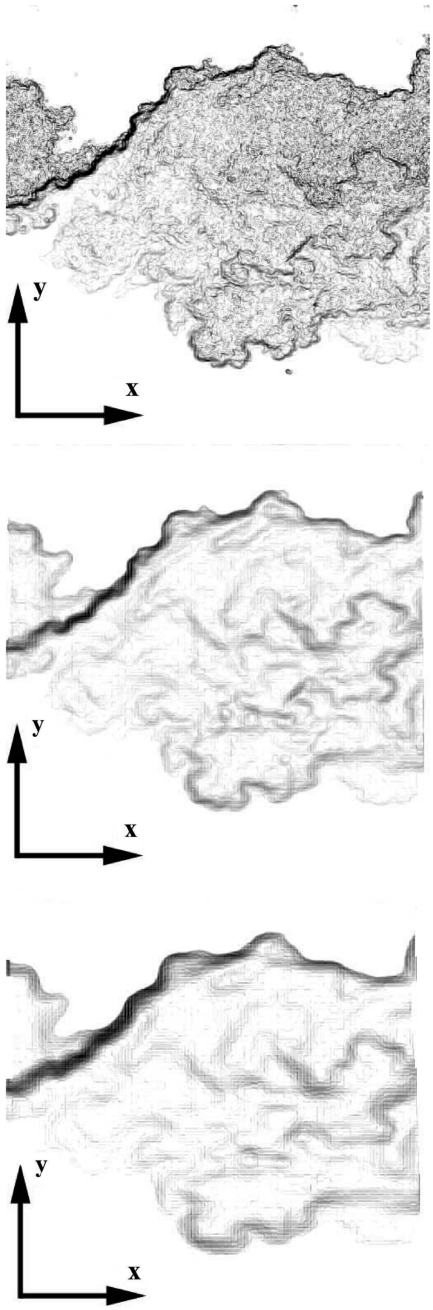

Fig. 4 Corresponding refractive-index interfaces shown for the shear-layer image and coarse-grained images. These images were generated from the original LIF images by computing the gradient of the refractive-index field throughout the shear layer. High-gradient refractive-index interfaces are shown as dark regions. Effects of multiresolution effects are seen in the number and strength of the interfaces.

An empirical relationship between the percent change in OPD_{rms} and the resolution-reduction factors can be found by looking at the log plots shown in Figs. 9 and 11. It can be seen that

$$\%\ \text{change in OPD}_{\text{rms}} = ke^{\gamma q} \tag{20}$$

where q is a specific resolution-reduction factor (q_1, q_2, etc.), and where k and γ are parameters that can be determined empirically, through use of a best-fit line, from the resolution-reduction data. In general, these two parameters can be expected to depend on the flow conditions. This relationship breaks down as the resolution-reduction factor approaches zero, because at that point there will be no change in the OPD_{rms}; however, the empirical relationship is demonstrated to hold for a wide range of resolution.

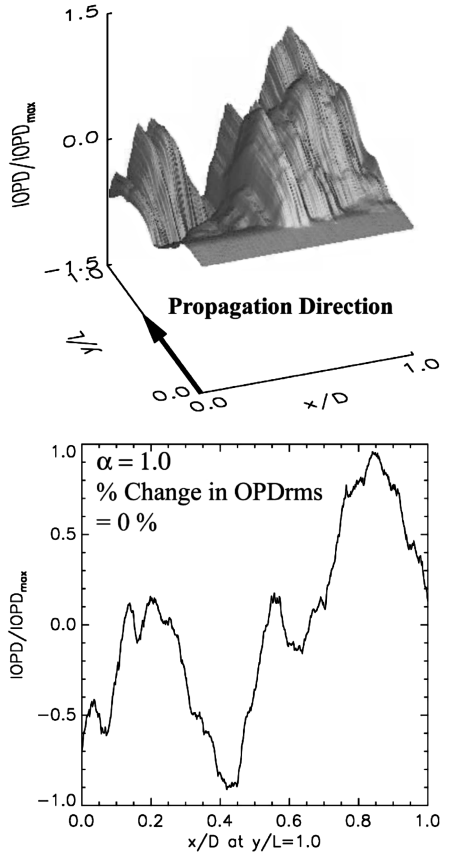

Fig. 5 IOPD surface plots shown for a shear-layer reference image with the corresponding OPD profile at the end of the shear layer. This image is approximately 800 by 800 pixels. Values of α and percent change in OPD_{rms} are defined by Eqs. (3) and (16), respectively.

In the context of aero-optical closed-loop applications (for example, adaptive optics combined with closed-loop flow control), one would prefer to be able to acquire space-time 4-D refractive-field information. Recall that in the current experimental setup, the beam, generated by an ultraviolet laser, is shaped into a laser sheet that is then propagated through the shear layer, producing a high-resolution 2-D image. To get a full 4-D picture of the flowfield, a 3-D image of the shear layer would need to be generated. To generate a 3-D image with a 2-D laser sheet would require sweeping the sheet at high speeds through the shear layer. The beam would need to be swept at a sufficiently fast rate to ensure that the flow would be sufficiently "frozen" at each plane to effectively generate a 3-D image. Currently, the ICCD camera used in these experiments can resolve images at a resolution of 1000 by 1000 pixels. To get a high-resolution 3-D image, for example, one would require the sheet to be swept through at least 1000 planar locations through the shear layer. This would, of course, require a very fast camera to capture this sweep. At each point in the sweep, the camera would have 1000 by 1000 (or 10^6) pixels of information. Therefore, the total number of pixels in a full 3-D image would be 10^9. Normal motion picture is captured at 30 frames per second. Therefore, 30×10^9 information pixels would need to be collected and analyzed each second. This adds up to 30 GB/s of data that need to be transferred, which is a substantial amount of bandwidth. Using our current resolution robustness data, it can be shown that the bandwidth for the 4-D experiment can be reduced substantially without significantly changing the results of the analysis. Using a lower-resolution camera of 100 by 100 pixels yields a 99% reduction of information, yet would not significantly affect the OPD_{rms} value. Creating an image with 100 by 100 by 100 pixels results in 10^6 pixels in the full 3-D image. Now, even if a 3-D image is captured every 10 ms, we would have 10^8 pixels of information a second, which equates to 100 MB/s of bandwidth. This is a much more reasonable value for information transfer with current

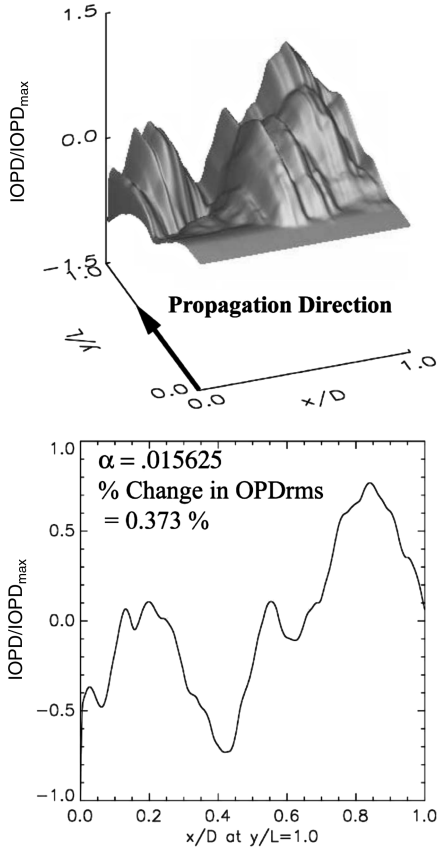

Fig. 6 IOPD surface plots shown for a shear-layer coarse-grained image with the corresponding OPD profile at the end of the shear layer. This image is approximately 100 by 100 pixels. Values of α and percent change in OPD_{rms} are defined by Eqs. (3) and (16), respectively.

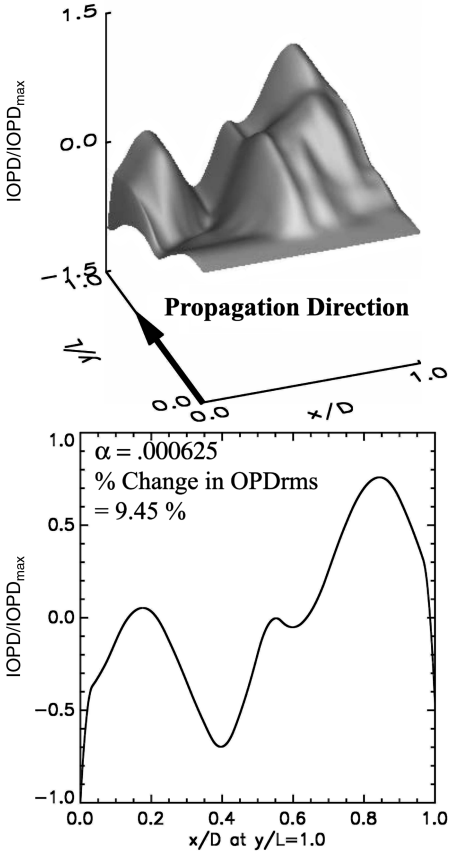

Fig. 7 IOPD surface plots shown for a shear-layer coarse-grained image with the corresponding OPD profile at the end of the shear layer. This image is approximately 20 by 20 pixels. Values of α and percent change in OPD_{rms} are defined by Eqs. (3) and (16), respectively.

and near-term foreseeable technology. Additionally, it can be noted that lower-resolution cameras can be made to operate faster than high-resolution cameras, due to the reduction of information needed to be processed and converted to digital signals, thereby allowing for faster capture rates to examine detailed temporal behavior of the turbulent shear layer.

Figures 5–7 demonstrate the presence of significant resolution robustness of shear-layer flowfields. Even at the lowest resolutions examined, the OPD_{rms} values are very close to the reference-resolution case. The present observations potentially have many practical applications with regard to imaging bandwidth requirements for successful closed-loop adaptive optics systems or bandwidth requirements for closed-loop flow-control systems, as well as promising applications for the computational community. In many closed-loop systems, there are issues created by bandwidth requirements for the transferring of aero-optical feedback data into the computational system. In adaptive optics systems, one needs accurate real-time optical data to change the parameters of the incident beam to improve the performance of the wave front through the flowfield. However, transferring large amounts of visual data, as stated before, requires high bandwidth, which is extremely expensive in many practical applications. Demonstration of resolution robustness allows for the use of lower-resolution cameras to capture optical data. Knowledge that a significantly lower-resolution image can essentially capture the primary aero-optical effects to a comparable extent as a high-resolution image can be expected to allow for significantly reduced bandwidth to be used by the adaptive optics system. This can allow for additional aero-optical feedback data to be collected or for images to be taken and transferred at a greater rate to further improve the closed-loop system.

In the computational aero-optics community [6,7,11,16,17], direct numerical simulations of turbulence and laser beam propagation are necessarily associated with high-node-value computations, which

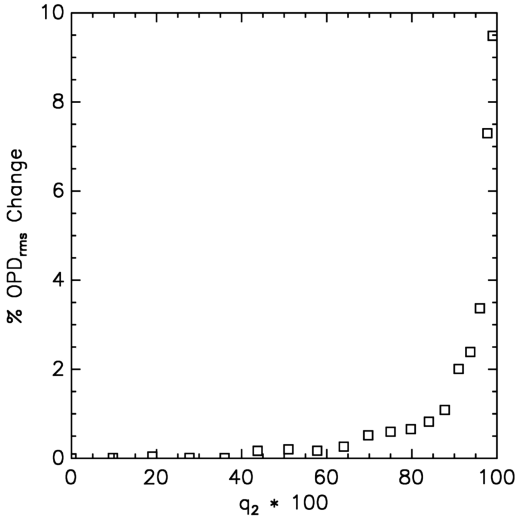

Fig. 8 Percent change OPD_{rms} vs the change in resolution of the 2-D image (q_2). This plot shows that even at low resolutions there is significant robustness in the OPD_{rms} value of the system.

are very expensive in terms of processor power and time. The present findings of aero-optical resolution robustness indicate the potential utility of reduced-resolution computational models. Large-eddy simulations [18], for example, with accurate subgrid-scale models, can thus be expected to be very useful in capturing aero-optical aspects of turbulence without a high number of computational grid points. By reducing the computational resolution, assuming a proper subgrid-scale model, one can therefore expect that the large-scale aero-optical interactions will be adequately simulated.

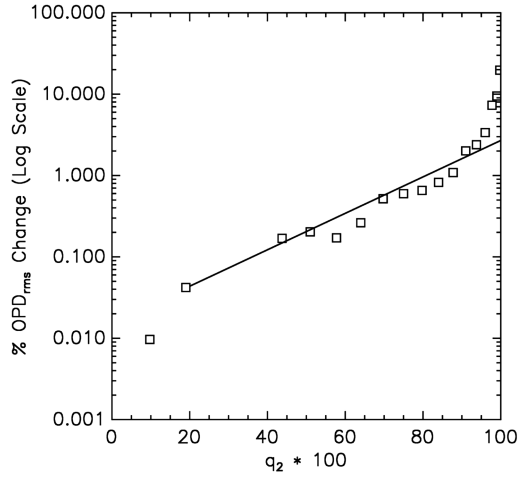

Fig. 9 Percent change OPD_{rms} (log scale) vs the change in resolution of the 2-D image (q_2). This plot shows that the robustness behavior exhibits approximately exponential scaling in a range of resolution-reduction factors. A best-fit line was created over the data to show the general trend. The best-fit line is described by Eq. (20), in which $k = 1.55 \times 10^{-4}$ and $\gamma = 5.15 \times 10^{-2}$.

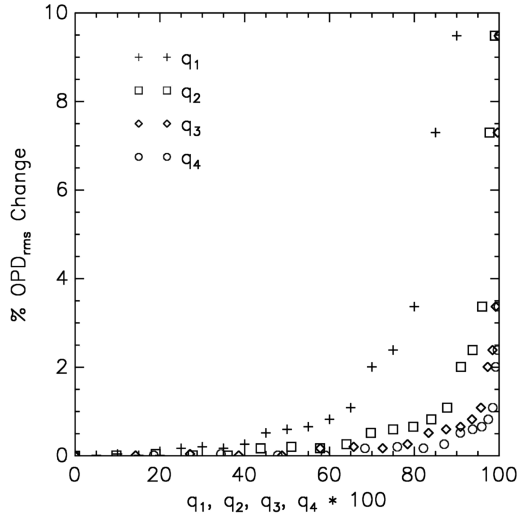

Fig. 10 Percent change OPD_{rms} vs the resolution-reduction parameters of the image. Values for q_1, q_3, and q_4 are estimated based on present data. This plot reveals that there is only weak dependence on resolution scale for a wide range of resolution-scale reduction factors.

IV. Conclusions

The effects of spatial imaging resolution on a computed aero-optical interaction parameter were examined using experimental images of the refractive-index field in turbulent compressible separated shear layers. Spatial coarse-graining of the high-resolution refractive-index images were conducted and the resulting aero-optical aberrations were evaluated. Evidence was presented for significant robustness of the aero-optical interactions to resolution changes. This demonstrates that the large scales of the turbulent refractive field are aero-optically dominant relative to the small scales. The extent to which the large scales dominate the small scales is quantified in terms of a measure of the aero-optical contributions as a function of scale.

The present work has a wide range of implications in the experimental, computational, and theoretical communities. Resolution robustness of aero-optical interactions can be expected to facilitate the reduction of bandwidth in closed-loop systems, the reduction of computational costs in simulations, and physical modeling of the dominant aero-optical effects. Even with the continuing advances in imaging capabilities, the benefits of

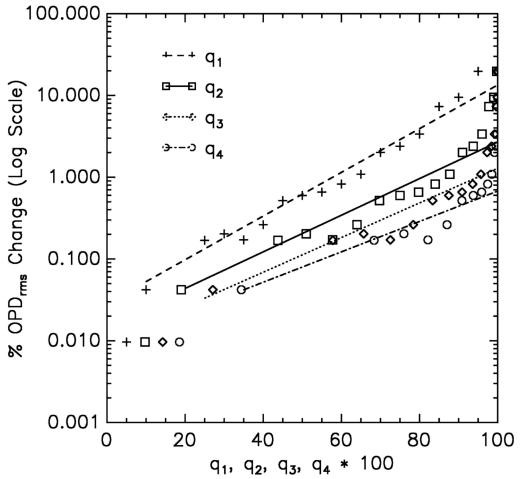

Fig. 11 Percent change OPD_{rms} (log scale) vs the resolution-reduction parameters of the image. Values for q_1, q_3, and q_4 are estimated based on present data; q_1 ($k = 2.85 \times 10^{-4}$ and $\gamma = 6.15 \times 10^{-2}$), q_2 ($k = 1.55 \times 10^{-4}$ and $\gamma = 5.15 \times 10^{-2}$), q_3 ($k = 9.78 \times 10^{-5}$ and $\gamma = 4.878 \times 10^{-2}$), and q_4 ($k = 9.38 \times 10^{-5}$ and $\gamma = 4.278 \times 10^{-2}$). A best-fit line was created over each set of OPD_{rms} values, indicating approximately exponential scaling. This plot indicates that there is strong robustness of the aero-optical aberrations to resolution scale in a wide range of resolution-scale reduction factors.

capturing the dominant aero-optical interactions with reduced resolution and bandwidth allow for greater flexibility in many applications. Similarly, even with the continuing advances in computational capabilities, the resolution robustness suggests the benefits of accurate large-eddy simulations as tools for capturing and analyzing the dominant aero-optical behavior.

Acknowledgments

We are grateful to S. Piatrovich and A. Freeman for their assistance with this study. We are also grateful to the Referees for their comments.

References

[1] Jumper, E. J., and Fitzgerald, E. J., "Recent Advances in Aero-Optics," *Progress in Aerospace Sciences*, Vol. 37, No. 3, 2001, pp. 299–339. doi:10.1016/S0376-0421(01)00008-2

[2] Catrakis, H. J., "Turbulence and the Dynamics of Fluid Interfaces with Applications to Mixing and Aero-Optics," *Recent Research Developments in Fluid Dynamics*, Vol. 5, Transworld Research Network, Kerala, India, 2004, pp. 115–158.

[3] Liepmann, H. W., "Deflection and Diffusion of a Light Ray Passing Through a Boundary Layer," Douglas Aircraft Co., Rept. SM-14397, Santa Monica, CA, 1952.

[4] Kyrazis, D., "Optical Degradation by Turbulent Free Shear Layers," *Optical Diagnostics in Fluid and Thermal Flow*, edited by S. S. Cha and J. D. Trolinger, Proceedings of SPIE–The International Society for Optical Engineering, Society of Photo-Optical Instrumentation Engineers, Bellingham, WA, 1993, pp. 170–181.

[5] Dimotakis, P. E., Catrakis, H. J., and Fourguette, D. C. L., "Flow Structure and Optical Beam Propagation in High-Reynolds-Number Gas-Phase Shear Layers and Jets," *Journal of Fluid Mechanics*, Vol. 433, 2001, pp. 105–134.

[6] Jones, M., and Bender, E. E., "CFD-Based Computer Simulation of Optical Turbulence Through Aircraft Flowfields and Wakes," 32nd AIAA Plasmadynamics and Lasers Conference, Anaheim, CA, AIAA Paper 2001-2798, June 2001.

[7] Tromeur, E., Garnier, E., Sagaut, P., and Basdevant, C., "Large Eddy Simulations of Aero-Optical Effects in a Turbulent Boundary Layer," *Journal of Turbulence*, Vol. 4, No. 5, 2003, pp. 1–22. doi:10.1088/1468-5248/4/1/005

[8] Fitzgerald, E. J., and Jumper, E. J., "The Optical Distortion Mechanism in a Nearly Incompressible Free Shear Layer," *Journal of Fluid Mechanics*, Vol. 512, 2004, pp. 153–189.

[9] Catrakis, H. J., and Aguirre, R. C., "New Interfacial Fluid Thickness Approach in Aero-Optics with Applications to Compressible

Turbulence," *AIAA Journal*, Vol. 42, No. 10, 2004, pp. 1973–1981.
[10] Zubair, F. R., and Catrakis, H. J., "Aero-Optical Interactions Along Laser Beam Propagation Paths in Compressible Turbulence," *AIAA Journal*, Vol. 45, No. 7, 2007, pp. 1663–1674. doi:10.2514/1.27342
[11] Truman, C. R., and Lee, M. J., "Effects of Organized Turbulence Structures on the Phase Distortion in a Coherent Optical Beam Propagating Through a Turbulent Shear Flow," *Physics of Fluids A*, Vol. 2, May 1990, pp. 851–857. doi:10.1063/1.857633
[12] Sreenivasan, K. R., "Fractals and Multifractals in Fluid Turbulence," *Annual Review of Fluid Mechanics*, Vol. 23, 1991, pp. 539–600. doi:10.1146/annurev.fl.23.010191.002543
[13] Thurber, M. C., and Hanson, R. K., "Pressure and Composition Dependences of Acetone Laser-Induced Fluorescence with Excitation at 248, 266, and 308 nm," *Applied Physics B (Lasers and Optics)*, Vol. 69, No. 3, 1999, pp. 229–240. doi:10.1007/s003400050799
[14] Piatrovich, S., and Catrakis, H. J., "Multiresolution Robustness of the Probability Density of Scalar Fields and Multiscale Aspects of Scalar Interfaces in Fully Developed Turbulent Jets," *Journal of Turbulence*, Vol. 8, No. 27, 2007, pp. 1–21. doi:10.1080/14685240701364858
[15] Born, M., and Wolf, E., *Principles of Optics: Electromagnetic Theory of Propagation, Interference and Diffraction of Light*, 7th ed., Cambridge Univ. Press, New York, 1999.
[16] Fleck, J. A., Jr., Morris, J. R., and Feit, M. D., "Time-Dependent Propagation of High Energy Laser Beams Through the Atmosphere," *Applied Physics*, Vol. 10, No. 11, 1976, pp. 129–160.
[17] Yahel, R. Z., "Turbulence Effects on High Energy Laser Beam Propagation in the Atmosphere," *Applied Optics*, Vol. 29, July 1990, pp. 3088–3095.
[18] Meneveau, C., and Katz, J., "Scale-Invariance and Turbulence Models for Large-Eddy Simulation," *Annual Review of Fluid Mechanics*, Vol. 32, 2000, pp. 1–32. doi:10.1146/annurev.fluid.32.1.1

J. Gore
Associate Editor